



Article

# Magnetic Properties and Magnetocaloric Effect of Polycrystalline and Nano-Manganites $\text{Pr}_{0.65}\text{Sr}_{(0.35-x)}\text{Ca}_x\text{MnO}_3$ ( $x \leq 0.3$ )

Roman Atanasov<sup>1</sup>, Dorin Ailenei<sup>1</sup>, Rares Bortnic<sup>1</sup>, Razvan Hirian<sup>1</sup>, Gabriela Souca<sup>1</sup>, Adam Szatmari<sup>1</sup>, Lucian Barbu-Tudoran<sup>2</sup> and Iosif Grigore Deac<sup>1,\*</sup>

- <sup>1</sup> Faculty of Physics, Babes-Bolyai University, Str. Kogalniceanu 1, 400084 Cluj-Napoca, Romania; atanasov.roman@ubbcluj.ro (R.A.); dorin.ailenei@stud.ubbcluj.ro (D.A.); rares.bortnic@ubbcluj.ro (R.B.); razvan.hirian@ubbcluj.ro (R.H.); gabriela.souca@ubbcluj.ro (G.S.); adam.szatmari@ubbcluj.ro (A.S.)
- <sup>2</sup> National Institute for Research and Development of Isotopic and Molecular Technologies, Str. Donath 67-103, 400293 Cluj-Napoca, Romania; lucian.barbu@itim-cj.ro
- \* Correspondence: iosif.deac@phys.ubbcluj.ro

**Abstract:** Here we report investigations of bulk and nano-sized  $\text{Pr}_{0.65}\text{Sr}_{(0.35-x)}\text{Ca}_x\text{MnO}_3$  compounds ( $x \leq 0.3$ ). Solid-state reaction was implemented for polycrystalline compounds and a modified sol-gel method was used for nanocrystalline compounds. X-ray diffraction disclosed diminishing cell volume with increasing Ca substitution in Pbnm space group for all samples. Optical microscopy was used for bulk surface morphology and transmission electron microscopy was utilized for nano-sized samples. Iodometric titration showed oxygen deficiency for bulk compounds and oxygen excess for nano-sized particles. Measurements of resistivity of bulk samples revealed features at temperatures associated with grain boundary condition and with ferromagnetic (FM)/paramagnetic (PM) transition. All samples exhibited negative magnetoresistivity. Magnetic critical behavior analysis suggested the polycrystalline samples are governed by a tricritical mean field model while nanocrystalline samples are governed by a mean field model. Curie temperatures values lower with increasing Ca substitution from 295 K for the parent compound to 201 K for  $x = 0.2$ . Bulk compounds exhibit high entropy change, with the highest value of 9.21 J/kgK for  $x = 0.2$ . Magnetocaloric effect and the possibility of tuning the Curie temperature by Ca substitution of Sr make the investigated bulk polycrystalline compounds promising for application in magnetic refrigeration. Nano-sized samples possess wider effective entropy change temperature ( $\Delta T_{\text{fwhm}}$ ) and lower entropy changes of around 4 J/kgK which, however, puts in doubt their straightforward potential for applications as magnetocaloric materials.

**Keywords:** manganites; nanoparticle perovskites; crystallography; magnetic behavior; phase transition; critical behavior; magnetocaloric effect



**Citation:** Atanasov, R.; Ailenei, D.; Bortnic, R.; Hirian, R.; Souca, G.; Szatmari, A.; Barbu-Tudoran, L.; Deac, I.G. Magnetic Properties and Magnetocaloric Effect of Polycrystalline and Nano-Manganites  $\text{Pr}_{0.65}\text{Sr}_{(0.35-x)}\text{Ca}_x\text{MnO}_3$  ( $x \leq 0.3$ ). *Nanomaterials* **2023**, *13*, 1373. <https://doi.org/10.3390/nano13081373>

Academic Editor: Julian Maria Gonzalez Estevez

Received: 19 March 2023

Revised: 10 April 2023

Accepted: 11 April 2023

Published: 14 April 2023



**Copyright:** © 2023 by the authors. Licensee MDPI, Basel, Switzerland. This article is an open access article distributed under the terms and conditions of the Creative Commons Attribution (CC BY) license (<https://creativecommons.org/licenses/by/4.0/>).

## 1. Introduction

Organic life is possible in a certain range of temperature because chemical exchange is destroyed above and below that range [1]. Throughout history, while artists were driven by the need to stay “cool”, the engineering part of the human brain kept searching for more practical solutions [2]. It is obvious that the best method for cooling our environment is the one that does not harm it. As such, magnetocaloric materials present a viable alternative to harmful gasses [3,4].

Magnetocaloric effect was reported in 1881 [5], but only recently has its potential for everyday use been discussed. Gadolinium Gd has been a forerunner in excellent magnetocaloric effect for a while, until its alloys were found to have higher values of entropy change [3]. They are expensive and require fields of over 5 T for operational use [4], and so the search for even more effective compounds has begun.

Compounds of the type  $\text{A}_{1-x}\text{B}_x\text{MnO}_3$  (where A is a trivalent rare earth cation and B is a divalent alkaline earth cation [6] (pp. 1–153) have a perovskite structure. They allow for

$\text{Mn}^{3+}$ -O- $\text{Mn}^{4+}$  interaction where an electron from  $\text{Mn}^{3+}$  can hop to  $\text{Mn}^{4+}$ , thus aligning the magnetic moments. Such interaction is named “double exchange” and is the main reason for their electric and magnetic properties [7] (pp. 18–21), [8] (pp. 167–293).

Recent work has shown that compounds such as  $\text{La}_{1-x}\text{Sr}_x\text{MnO}_3$  and  $\text{Pr}_{1-x}\text{Ba}_x\text{MnO}_3$  [9,10] exhibit large magnetic entropy change. Structurally, a divalent  $\text{Sr}^{2+}$  and  $\text{Ba}^{2+}$  are doped in place of trivalent  $\text{La}^{3+}$  and  $\text{Pr}^{3+}$ . The strongest “double exchange” interaction results are achieved at the doping level of about  $x = 0.3$  [8]. Further introduction of divalent elements leads to antiferromagnetic (AFM) arrangement and can cause localization of charge—the so-called charge ordered (CO) state [11]. Because of this, further substitution of trivalent or divalent ions with different size ions can change the structure, volume and the magnetic properties.

In this work, we have prepared polycrystalline and nanocrystalline samples of  $\text{Pr}_{0.65}\text{Sr}_{0.35-x}\text{Ca}_x\text{MnO}_3$  ( $x = 0.02, 0.05, 0.1, 0.2, 0.3$ ). Magnetic properties of the parent bulk compound  $\text{Pr}_{0.65}\text{Sr}_{0.35}\text{MnO}_3$  have been reported previously in the literature [12].  $\text{Ca}^{2+}$  ions act as the substitute for divalent  $\text{Sr}^{2+}$  ions in order to bring  $T_C$  down from 295 K of the parent compound  $\text{Pr}_{0.65}\text{Sr}_{0.35}\text{MnO}_3$  [12] in bulk and  $T_C = 257$  K of nano-sized compounds. Systems were crystallographically and morphologically investigated by X-ray diffraction (XRD), optical microscopy and transmission electron microscopy (TEM), and Rietveld refinement analysis of XRD. Stoichiometry [13] and structure [8,9] of the samples greatly affects properties. Preparation method can affect stoichiometry of the compounds, sometimes causing accidental vacancies in  $\text{Pr}^{3+}$  ions. Some changes in magnetic and electrical behavior, therefore, could be observed, but are unquantifiable by this experiment. Additionally, oxygenation plays an important role in final measurements. Oxygen deficiency and excess change stoichiometry of the compounds by changing  $\text{Mn}^{3+}/\text{Mn}^{4+}$  ratio electrical conductivity and overall magnetization. In our work, oxygen content was investigated by chemical analysis of Iodometry. Critical behavior was analyzed by construction of modified Arrott plots (MAP), which was also confirmed by the Kouvel–Fisher (KF) method. Nanocrystalline compounds have lower maximum entropy change values but much wider effective temperature range. Electrical measurements, in the bulk samples, revealed colossal magnetoresistance behavior [11,14,15].

This paper is organized as follows: in Section 2 we describe the preparation methods, as well as all the characterization methods we used in structural, morphological, oxygen stoichiometric, electrical, and magnetic investigation. In Section 3 we present the results of our investigation, analysis of data, and we discuss the magnetic critical behavior, electrical and magnetic properties of our samples. Finally, we summarize our results in Section 4.

## 2. Materials and Methods

Polycrystalline samples were prepared by conventional solid-state reaction. High purity oxides of principal elements  $\text{Pr}_6\text{O}_{11}$ ,  $\text{SrO}$ ,  $\text{MnO}_2$ , and carbonate  $\text{CaCO}_3$  were purchased from Alfa Aesar (Heysham, UK). After being mixed by hand in a mortar for 3 h, the powders were calcinated at 1100 °C for 24 h in air. Later, the powder was pressed into a pellet at 3 tons and sintered in air at 1350 °C for 30 h.

Nanocrystalline samples were prepared by sucrose sol-gel method. Nitrates  $\text{Pr}(\text{NO}_3)_3 \cdot 6\text{H}_2\text{O}$ ,  $\text{Sr}(\text{NO}_3)_2$ ,  $\text{Ca}(\text{NO}_3)_2 \cdot 4\text{H}_2\text{O}$ , and  $\text{Mn}(\text{NO}_3)_2 \cdot 6\text{H}_2\text{O}$  were dissolved in pure water ( $18.2 \text{ M}\Omega \times \text{cm}$  at 25 °C) for up to 1 h at 60 °C after which, 10 g of sucrose was added. This enables positive ions to attach themselves to OH hubs of the sucrose chain. After stirring for 45–60 min temperature was turned down to room temperature. Two grams of pectin was added to expand the xero-gel and mixed for further 20 min. Solutions were dried at 200 °C for 24 h or until all water evaporated. Finally, gels were burned at 1000 °C for 2 h to obtain the nano-sized particles. If the reaction does not happen, as was the case in this experiment, some small amount of Acetic acid can be added to the mix at the last stage before drying in order to bring the chains closer together. However, such action usually results in somewhat bigger particles.

X-ray diffraction (XRD) was implemented for structural categorization of all samples. Optical microscopy was used on bulk samples for grain size determination and surface defects. Transmission electron microscopy (TEM) allowed for nanocrystalline particle size determination. Analysis of XRD data was performed by Rietveld refinement method, as well as Williamson–Hall (W-H) method.

Iodometric analytical titration was applied in order to detect deficiency or excess of oxygen in the samples. A small amount of a sample was placed in a closed vessel containing hydrochloric acid (HCl) where positive  $Mn^{4+}$  ions react with  $Cl^{-}$  to produce  $Cl_2$ . An inert gas pushes  $Cl_2$  into another vessel containing potassium iodide (KI) where it reacts to produce  $I_2$ . This mixture was titrated with sodium thiosulfate and the ratio of  $Mn^{3+}$  to  $Mn^{4+}$  was calculated by the stoichiometry of balanced chemical equations [16].

Electrical properties were found using the four-point technique in a cryogen-free superconducting setup. Four-point chips, measuring voltage and current separately were placed in applied magnetic fields of up to 5 T with a varied temperature between 10 K and 300 K. Resistance of the samples was recorded, resistivity was calculated using sample dimensions.

Magnetic measurements were made using a Vibrating Sample Magnetometer (VSM) in the temperature range of 4–300 K in external magnetic fields of up to 4 T.

### 3. Results

#### 3.1. Structural Analysis

Visual inspection of stack XRD patterns, as shown in Figure 1, suggests possible decrease in cell dimensions due to the shift to the right of patterns with increasing Ca content. All samples are single phase with less than 5% levels of impurities. Wider peaks for nanocrystalline samples are indicative of smaller crystallites size in the compounds [17] which is further confirmed by Rietveld refinement analysis and Williamson–Hall method in Tables 1 and 2.

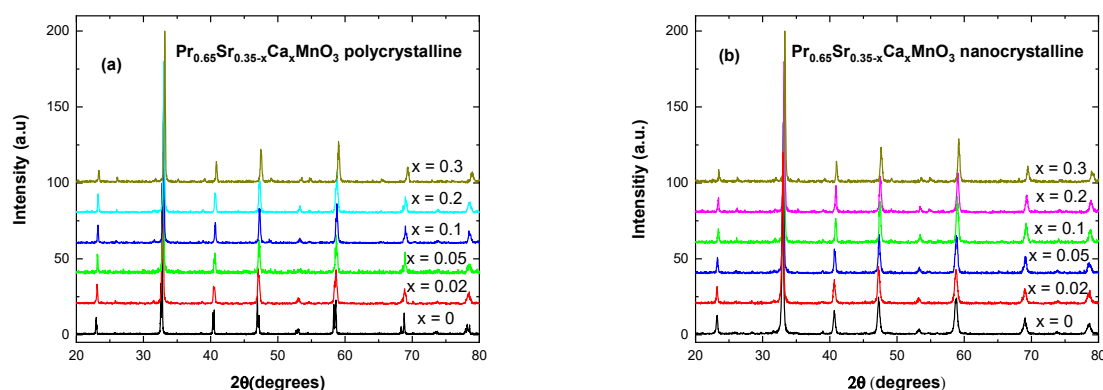


**Figure 1.** X-ray diffraction patterns for (a)  $Pr_{0.65}Sr_{0.35-x}Ca_xMnO_3$  polycrystalline bulk samples and (b)  $Pr_{0.65}Sr_{0.35-x}Ca_xMnO_3$  nano-sized samples.

**Table 1.** Calculated tolerance factors, Mn–O lengths, and crystallite sizes for polycrystalline samples using the Williamson–Hall and Rietveld methods and including particle diameters by optical microscopy.

Ca Content (Bulk)	<i>t</i> (Tolerance Factor)	Mn–O (Å)	Mn–O–Mn (°)	Average Particle Diameter (µm)	Williamson–Hall Size (nm)	Average Rietveld Size (nm)	Strain
x = 0.02	0.925	1.964	157.73	15	111.33	96.67	0.0022
x = 0.05	0.924	1.962	157.74	11	156.63	113.68	0.0019
x = 0.1	0.921	1.961	157.73	13	132.88	192.59	0.0024
x = 0.2	0.917	1.956	157.69	10	144.85	125.64	0.0023
x = 0.3	0.912	1.954	157.72	11	123.56	86.79	0.0021

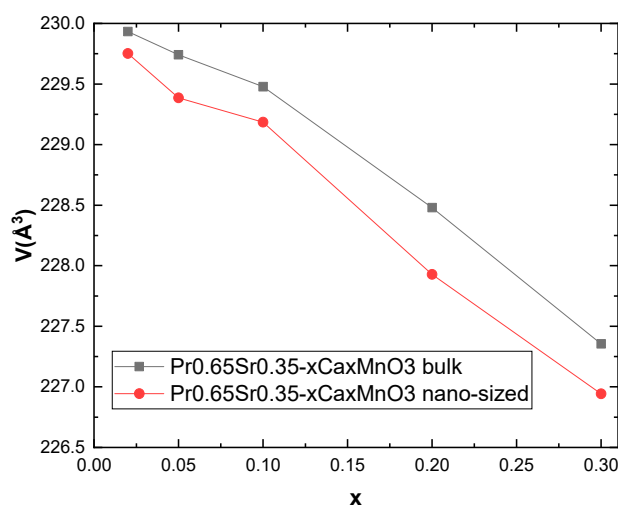
**Table 2.** Calculated Mn–O lengths and crystallite sizes for nanocrystalline samples using the Williamson–Hall and Rietveld methods and including grain diameters from TEM.

Ca Content (Nano)	Mn–O (Å)	Mn–O–Mn (°)	Average Particle Diameter (nm)	Williamson–Hall Size (nm)	Average Rietveld Size (nm)	Strain
x = 0	1.972	157.74	68.1	72.45	54.33	0.0018
x = 0.02	1.964	157.75	64.8	71.15	45.64	0.0019
x = 0.05	1.958	157.69	78.2	84.59	57.21	0.0016
x = 0.1	1.957	157.69	87.5	82.95	39.75	0.0019
x = 0.2	1.955	157.7	71.5	66.73	45.62	0.0017
x = 0.3	1.951	157.71	65.7	69.69	51.11	0.002

Investigation of XRD data by Rietveld refinement analysis established orthorhombic (Pbnm) space group no. 62 for all samples, with decreasing cell dimensions and volume for each subsequent substitution of Sr. The results are illustrated in Figure 2. Stability of the structure in orthorhombic perovskite materials is assessed by the Goldschmidt tolerance factor. It was calculated using following relation [18,19]:

$$t = \frac{R_A + R_O}{\sqrt{2}(R_B + R_O)}, \quad (1)$$

where  $R_A$  is the radius of A cation,  $R_B$  is the radius of B cation, and  $R_O$  is the radius of the anion. All samples fall within orthorhombic/rhombohedral tolerance range of 0.7–1 [20] (pp. 707–714).

**Figure 2.** Plot of cell volume change for polycrystalline and nanocrystalline samples.

An addition of smaller crystal radius  $\text{Ca}^{2+}$  (1.32 Å) atoms in place of  $\text{Sr}^{2+}$  (1.45 Å) into the structure increases disorder [8,19] and decreases average Mn–O bond length, as seen in Tables 1 and 2, which plays a crucial role in “double exchange” interaction [8]. The average angle between Mn–O–Mn stays relatively the same throughout the range of substitutions at 157.72(3)°.

The Williamson–Hall (W-H) method is advantageous in that it takes into account strain between crystallites, as opposed to the Scherrer method, which does not [21]. Thus, results from W-H analysis are expected to be closer to the real values. A comparison between Rietveld refinement analysis and Williamson–Hall method for approximation of crystallite size can be performed by contrasting them with TEM and optical microscopy results. As can be observed in Table 1 for bulk samples, W-H and Rietveld results are similar, but are

two orders of magnitude different from real values. This can be attributed to each grain containing many crystallites. In Table 2, for nano-sized samples, it can be seen that values from W-H calculations are on average larger than those performed by Rietveld analysis and closer to values from TEM. Real sizes for nanocrystalline particles are in the upper limit of nano dimensions at approximately 70–80 nm. Selected samples of optical microscope pictures are presented in Figure 3 and selected TEM pictures in Figure 4.

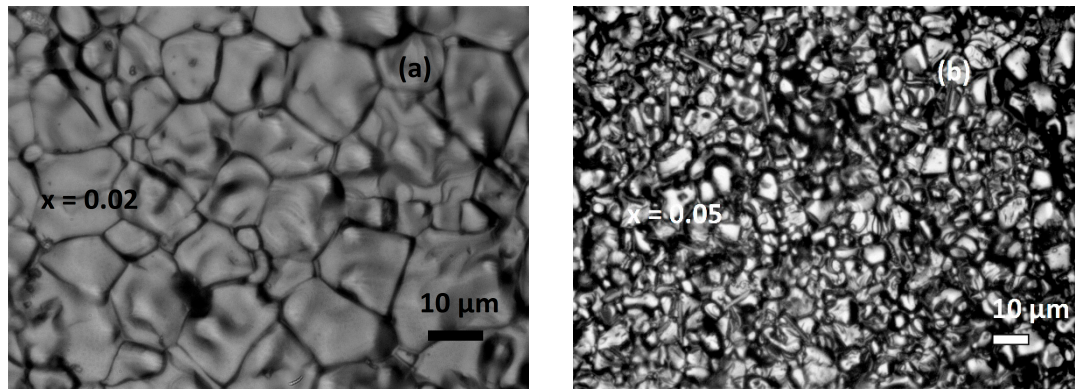


**Figure 3.** Selected optical microscope pictures for  $\text{Pr}_{0.7}\text{Sr}_{0.3-x}\text{Ca}_x\text{MnO}_3$  bulk samples (a) for  $x = 0.02$ , (b)  $x = 0.05$ .

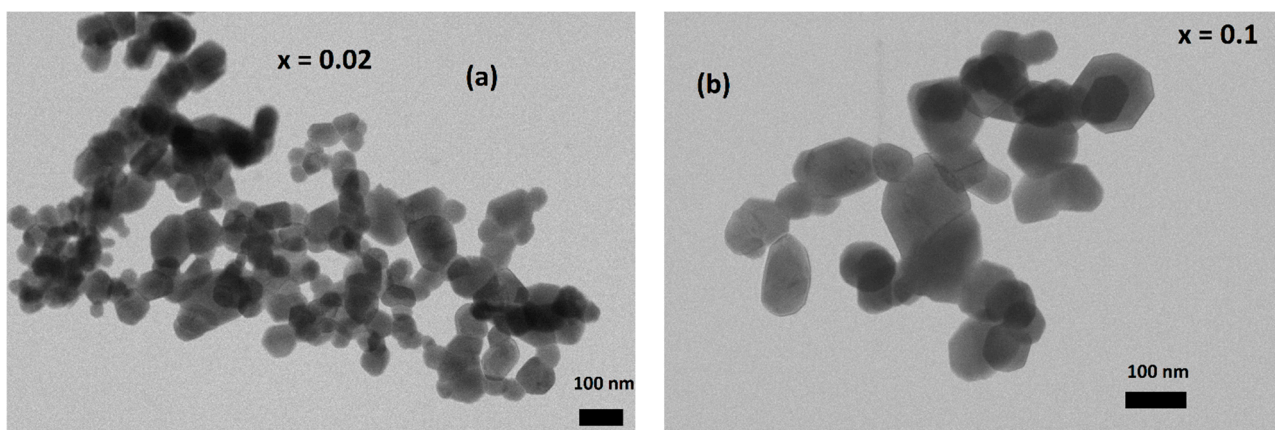


**Figure 4.** Selected TEM pictures for  $\text{Pr}_{0.7}\text{Sr}_{0.3-x}\text{Ca}_x\text{MnO}_3$  nano-sized samples for  $x = 0.02$  (a),  $x = 0.01$  (b).

### 3.2. Oxygen Content

Implementation of iodometric titration analysis for samples is a reliable method for determining deficiency or excess of oxygen in manganites [13,16]. All results are presented in Table 3.

Titration of bulk compounds revealed oxygen deficiency for all samples. An average of  $\text{O}_{2.93 \pm 0.02}$  for  $x = 0.02$ , similar to other samples, shows larger than expected deficiency of approximately  $\text{O}_{2.98}$  [22]. This is attributed to preparation methods and difficulty in oxygenating the sample during calcination and sintering. Lower levels of oxygen would affect magnetic and electrical properties as it affects the stoichiometry and changes  $\text{Mn}^{3+}/\text{Mn}^{4+}$  ratio which would lower the amount of “double exchange” interaction [13].

All nanocrystalline compounds exhibited small excess of oxygen stoichiometry. The level of excess did not exceed  $\text{O}_{3.02 \pm 0.01}$  as is with  $x = 0.02$  sample. We suggest that the culprit for such result should be found in the high surface to volume ratio of nano-sized particle. Broken bonds on the surface will increase the ratio of  $\text{Mn}^{4+}$  to  $\text{Mn}^{3+}$  by attracting oxygen in the air. This, in turn, can create vacancies and affect its magnetic and electrical properties.

**Table 3.** Average oxygen content calculated using iodometry for bulk and nanocrystalline samples.

Ca Content	Average Mn <sup>3+</sup> /Mn <sup>4+</sup> Ratio	Standard Deviation	Relative Standard Deviation (%)	Average Oxygen Content
x = 0.02 bulk	0.788	0.0167	2.12	O <sub>2.93±0.02</sub>
x = 0.05 bulk	0.783	0.0121	1.55	O <sub>2.93±0.01</sub>
x = 0.1 bulk	0.778	0.0139	1.79	O <sub>2.94±0.02</sub>
x = 0.2 bulk	0.781	0.0182	2.33	O <sub>2.94±0.02</sub>
x = 0.3 bulk	0.765	0.0226	2.95	O <sub>2.94±0.02</sub>
x = 0 nano	0.624	0.008	1.28	O <sub>3.01±0.01</sub>
x = 0.02 nano	0.612	0.009	1.47	O <sub>3.02±0.01</sub>
x = 0.05 nano	0.622	0.011	1.33	O <sub>3.01±0.01</sub>
x = 0.1 nano	0.615	0.009	1.77	O <sub>3.02±0.01</sub>
x = 0.2 nano	0.633	0.008	1.26	O <sub>3.01±0.01</sub>
x = 0.3 nano	0.638	0.012	1.88	O <sub>3.01±0.01</sub>

Finally, it can be observed that standard deviation, or deviation from the “mean”, is larger for bulk samples than the nano-sized samples. This is explained by the variation of oxygenation within the bulk. Nevertheless, all relative standard deviations do not exceed 3% and can be considered reliable.

### 3.3. Electrical Measurements

An investigation of electrical behavior for polycrystalline samples  $x = 0.02; 0.05; 0.1$  and  $0.2$  was performed using the four-point probe method in external fields of  $\mu_0 H = 0$  T;  $1$  T;  $2$  T in temperature range of  $10$ – $290$  K. For the sample with  $x = 0.3$  fields of up to  $5$  T were used. Data were used to estimate metal–insulator transition temperature  $T_p$  and magnetoresistivity  $MR$  according to the following equation [23]:

$$MR\% = [(q(H) - q(0))/q(0)] \times 100, \quad (2)$$

The first observation to be made is that all samples, except  $x = 0.3$ , exhibit a transition temperature  $T_{p1}$  typically associated with grain boundary conditions [23–25]. Visual inspection shows that it is a wide and smooth transition, different from the usual sharp peaks associated with ferromagnetic–paramagnetic transition (and consequently metal–insulator) at  $T_{p2}$  (inside of the grains). The addition of Ca ions increases disorder, which tends to spread itself toward the edges of the grains in order to conserve energy [26,27]. Boundaries act as insulators or semi-conductors [27,28]. As can be seen in Figure 5, the application of external field shifts  $T_p$  to the right. This is caused by lowering spin fluctuations and delocalization of charge carriers [19].

A separation between  $T_{p1}$  and  $T_{p2}$  (which is associated with  $T_C$ ) is reported when grain boundary conditions are strong enough due to mismatch in ionic radius at the A-site [26]. Samples  $x = 0.02$  and  $0.05$  do not show a peak  $T_{p2}$  because it is beyond the temperature range. Starting with  $x = 0.1$  a sharp peak appears which lies higher in temperature than  $T_C$  value. With application of a field,  $T_{p2}$  tends to smooth out, as can be seen with the sample  $x = 0.2$  in Figure 5b.

Special attention should be paid to the sample with  $x = 0.3$ . Its graph is presented in Figure 5c. Magnetic fields of up to  $5$  T were applied. For  $\mu_0 H = 0$  T;  $1$  T the sample conductivity is below the detection level for temperatures below  $50$  K. With the application of  $2$  T resistivity drops significantly. Its curve can be seen in the main portion of the figure. Curves for fields of  $3$ – $5$  T can be seen in the inset and show further drop in resistivity and a shift to higher temperatures for the peak. This suggests that higher

field overcomes intergrain resistance and further increase in the field induces a parallel alignment of manganese ions. In higher applied magnetic fields, the magnetic moments of the neighboring grains tend to be parallel, enhancing the tunneling of the conduction electrons similarly with a giant magnetoresistance effect (GMR) [26].

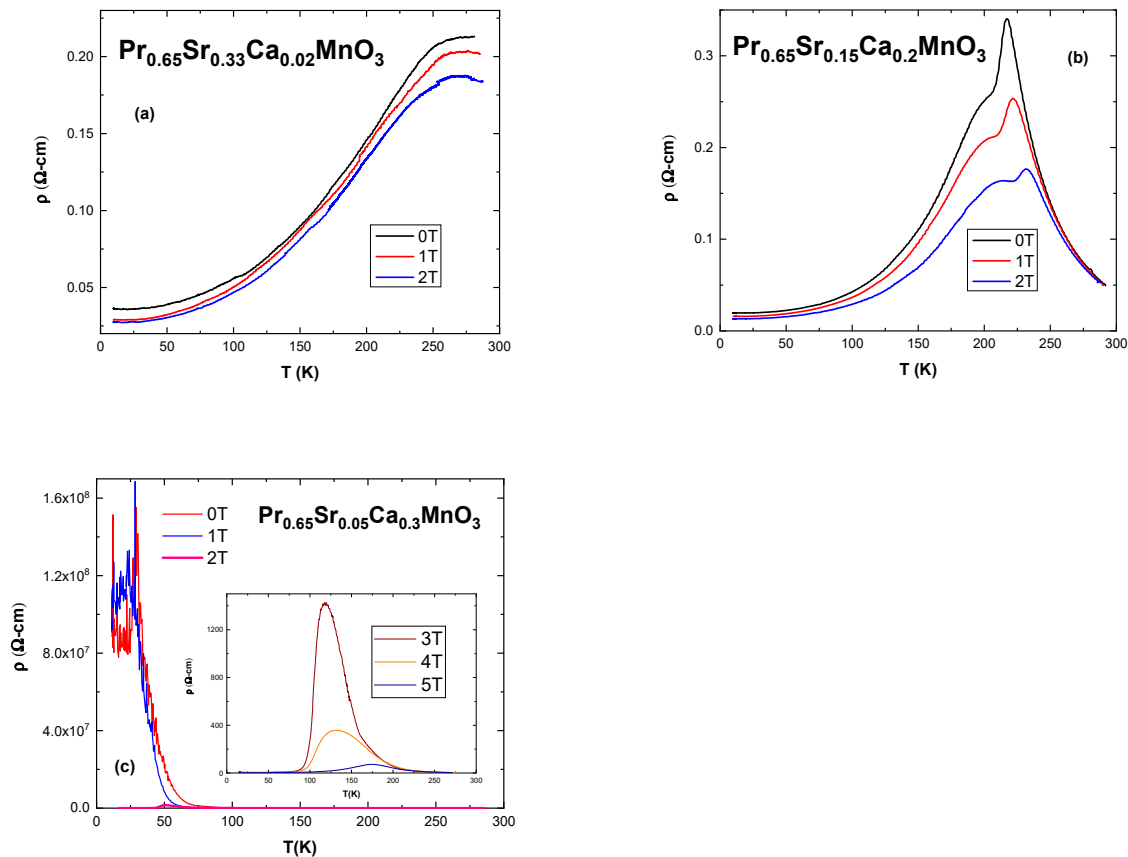


**Figure 5.** Graphs of resistivity vs. temperature for bulk samples: (a)  $x = 0.02$ , (b)  $x = 0.2$ , (c)  $x = 0.3$ ; The inset shows plot of resistivity at higher fields which are not visible in the main plot.

Magnetoresistivity is negative in all samples. Table 4 shows an increasing value of MR with increasing level of Ca substitution. The highest  $MR_{Max}$  (2 T) is 51.96% and 29.08% for 1 T for  $x = 0.2$  at 217 K. Sample with  $x = 0.02$  exhibits the lowest  $MR_{Max}$  of 11.9% and 4.45% for 2 T and 1 T at 289 K, respectively. A sample with  $x = 0.3$  has MR of 77.62% between 3 T and 4 T at 118 K and 99.99% for 2–3 T at 130 K (shown in brackets in Table 4). In order to calculate MR, both the peak value of resistivity from the lower field data and an isothermal value from the higher field data are taken and then inserted into Equation (2). The highest peak resistivity  $\rho_{peak}$  of about 3  $\Omega\text{cm}$  at 275 K is observed in sample  $x = 0.05$ . The lowest  $\rho_{peak}$  for  $x = 0.3$  at 5 T is 73  $\Omega\text{cm}$  (in brackets) at 174 K. All relevant data, including  $T_C$  and  $T_p$ , are presented in Table 4.

**Table 4.** Experimental values for  $\text{Pr}_{0.65}\text{Sr}_{0.35-x}\text{Ca}_x\text{MnO}_3$  bulk materials: electrical properties.

Compound (Bulk)	$T_C$ (K)	$T_{p1}$ (K) ( $T_{p2}$ (K))	$\rho_{peak}$ ( $\Omega\text{cm}$ ) in 0 T	$MR_{Max}$ (%) (1 T)	$MR_{Max}$ (%) (2 T)
$\text{Pr}_{0.65}\text{Sr}_{0.33}\text{Ca}_{0.02}\text{MnO}_3$	273	274	0.213	4.45	11.99
$\text{Pr}_{0.65}\text{Sr}_{0.3}\text{Ca}_{0.05}\text{MnO}_3$	261	273	3.094	12.28	22.75
$\text{Pr}_{0.65}\text{Sr}_{0.25}\text{Ca}_{0.1}\text{MnO}_3$	244	256 (258)	1.602	23.28	33.27
$\text{Pr}_{0.65}\text{Sr}_{0.15}\text{Ca}_{0.2}\text{MnO}_3$	201	210 (217)	0.341	29.08	51.96
$\text{Pr}_{0.65}\text{Sr}_{0.05}\text{Ca}_{0.3}\text{MnO}_3$	-	-	$>100 \times 10^8$ (72.985 in 5 T)	77.62 (between 3 and 4 T)	99.99 (between 2 and 3 T)

### 3.4. Magnetic Properties

Investigation of magnetization vs. temperature ( $M$  vs.  $T$ ), with the samples cooled in zero and in an applied magnetic field of  $\mu_0 H = 0.05$  T (ZFC-FC) was carried out in a vibrating sample magnetometer (VSM). All samples except  $x = 0.3$  exhibit strong ferromagnetic behavior. Samples with  $x = 0.3$  for both systems exhibit antiferromagnetic charge-exchange-type (CE-AFM) and charged ordered (CO) state. In CE-AFM structure,  $Mn^{3+}$  and  $Mn^{4+}$  are arranged like a checkerboard in the  $ab$ -plane ( $Mn-O_2$ ); exchange interaction causes  $Mn^{3+}$   $e_g$  electron to occupy either  $d_{3 \times 2-r_2}$  or  $d_{3y^2-r_2}$  orbital. As a result, there are FM zig-zag chain arrangements which are AFM to each other and also stack antiferromagnetically in the  $c$ -plane. Figure 6 presents selected graphs of  $M$  vs.  $T$  with insets representing a derivative  $dM/dT$  of the plots for which the minimum is associated with  $T_C$ . The addition of  $Ca^{2+}$  ions causes smaller cell dimensions; increased disorder and it lowers the Curie temperature [17]. The increase in Ca substitution lowers  $T_C$  further. Nano-sized particles show lower values of  $T_C$  than their bulk counterpart due to their size and surface effect, including broken bonds, canted spins, and reduced magnetization [29,30]. In addition, the curves for nano-sized samples are “smoother”, covering a wider temperature range in their ferromagnetic–paramagnetic change but have lower maximum value of magnetization  $M(T)$ .

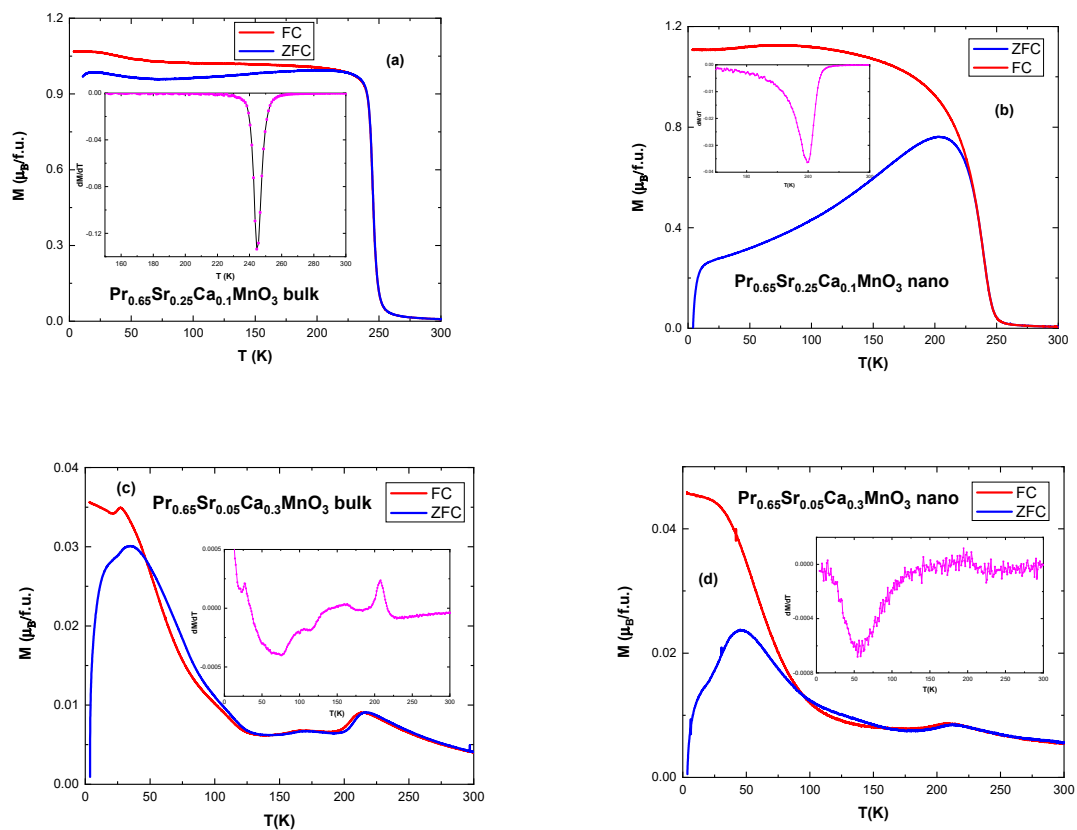


**Figure 6.** ZFC-FC plots in external field of 0.05 T (a) ZFC-FC curves and derivative of magnetization (inset) for the bulk sample  $Pr_{0.65}Sr_{0.25}Ca_{0.1}MnO_3$ ; (b) ZFC-FC curves and derivative (inset) for nanocrystalline sample  $Pr_{0.65}Sr_{0.25}Ca_{0.1}MnO_3$ . (c) ZFC-FC curves and derivative shown as inset, for polycrystalline sample  $Pr_{0.65}Sr_{0.05}Ca_{0.3}MnO_3$ ; (d) ZFC-FC curves and derivative shown in the inset for nanocrystalline sample  $Pr_{0.65}Sr_{0.05}Ca_{0.3}MnO_3$ .

An observation of ZFC-FC curves, especially for bulk samples, reveals an upturn in magnetization at lower temperatures at around 70–100 K, an example of which is in Figure 6a. This can be attributed to the magnetization of praseodymium Pr ions [10]. Samples with  $x = 0.3$  also exhibit increased magnetization at low temperatures starting

at around 100 K, seen in Figure 6c,d. Maximum value is not as high as for the rest of the samples, approximately  $0.04 \mu_B/\text{f.u.}$  for  $x = 0.3$  vs.  $1 \mu_B/\text{f.u.}$  for  $x = 0.1$ . Other CO compounds, such as  $\text{La}_{0.4}\text{Ca}_{0.6}\text{Mn}_{0.9}\text{Ga}_{0.1}\text{O}_3$  [11] and  $\text{Pr}_{0.75}\text{Na}_{0.25}\text{MnO}_3$  [14] have been reported with similar increase in magnetization due to suppression of CO state. The difference between  $\text{La}^{3+}$  and  $\text{Pr}^{3+}$  is their crystal ionic size ( $1.356 \text{ \AA}$  for  $\text{La}^{3+}$  and  $1.319 \text{ \AA}$  for  $\text{Pr}^{3+}$  [20]) and their electron configuration:  $\text{La}^{3+}$  has no  $4f$  electrons while  $\text{Pr}^{3+}$  has the configuration =  $[\text{Xe}]4f^2$ . The size difference affects the bandwidth, with Pr-based manganites being referred to as narrow bandwidth manganites. Appearance of the charged ordered state is influenced by  $\text{Mn}^{3+}/\text{Mn}^{4+}$  ratio as well as the bandwidth [31], therefore Pr based manganites enter CO state more easily. The low temperature increase in magnetization is associated with phase separation (PS), i.e., existence of FM clusters, forming among AFM matrix [11]. The graphs for  $x = 0.3$  at higher temperatures show behavior typical of charged ordered state. A small feature at around 170 K represents Neél temperature,  $T_N$  (most visible in the bulk sample), and the peak at around 210 K representing the onset of the charge ordering phase,  $T_{CO}$ . Such a behavior was revealed in several manganites systems such as  $\text{La}_{0.250}\text{Pr}_{0.375}\text{Ca}_{0.375}\text{MnO}_3$  [32],  $\text{Pr}_{0.7}\text{Ca}_{0.3}\text{MnO}_3$  [33],  $\text{La}_{0.3}\text{Ca}_{0.7}\text{Mn}_{0.8}\text{Cr}_{0.2}\text{O}_3$  [34],  $\text{Pr}_{0.57}\text{Ca}_{0.41}\text{Ba}_{0.02}\text{MnO}_3$  [35],  $\text{Nd}_{0.5}\text{Ca}_{0.5}\text{MnO}_3$  [36], and  $\text{La}_{0.4}\text{Ca}_{0.6}\text{MnO}_3$  [37], and it arises as a result of doping and/or due to the reducing of the sizes of the particles to the range of nanometers.

The feature from 45 K, in bulk sample, could be the signature of the blocking of isolated spins between FM clusters as seen in spin glass materials [38,39].

According to Landau's mean field theory [40], Gibbs free energy of the system around a critical point can be expanded in a Taylor series as:

$$G(T, M) = G_0 + MH + aM^2 + bM^4 + \dots, \quad (3)$$

where coefficients  $a$  and  $b$  depend on temperature. A derivative of the energy with respect to magnetization, to find the minima, results in an expression:

$$H/M = 2a + 4bM^2, \quad (4)$$

An easy way to confirm the correctness of the mean field theory approach for given samples is the Arrott plot, i.e.,  $M^2$  vs.  $H/M$  [41]. If isotherms are straight and parallel to each other around  $T_C$  then the assumption is correct. Observation of Arrott plots for our samples reveals curved, non-parallel lines for bulk compounds (Figure 7a,c) and almost straight lines for nano-sized compounds (Figure 7b,d). Furthermore, Banerjee criterion is a useful tool for determining the order of the phase transition [42]. According to the criterion, positive slope represents second order phase transition and negative slope corresponds to first order transition. Samples with  $x = 0, 0.02, 0.05, 0.1$  show only positive slope. As can be seen in Figure 7c,d, samples with  $x = 0.2$  show negative slope in the first stage of the magnetization at temperatures above  $T_C$  suggesting first order transition. Samples with  $x = 0.3$ , not pictured, show mostly negative slope plots.

Inexactness of the exponents in the Equation (4) can be solved by constructing an Arrott–Noakes plot, i.e.,  $M^{1/\beta}$  vs.  $\mu_0 H/M^{1/\gamma}$  [43] with proper exponents  $\beta$  and  $\gamma$ . The exponent  $\beta$  relates to the spontaneous magnetization below  $T_C$  and  $\gamma$  relates to the inverse susceptibility above  $T_C$  [44] (pp. 7–10). An additional exponent  $\delta$  relates magnetization and external field at  $T_C$ . In mean field model:  $\beta = 0.5$  and  $\gamma = 1$ , but there exist more models with different exponent values. The value of the exponents relates to the system dimensionality, spin, and range of the interaction  $J(r)$ . In renormalization group theory [45], exchange interaction is defined as  $J(r) = 1/r^{d+\sigma}$  where  $d$ —dimensionality of the system and  $\sigma$ —range of interaction. For  $\sigma$  greater than 2:  $\beta = 0.355$ ,  $\gamma = 1.366$  and  $\delta = 4.8$ —is the case of the 3D Heisenberg model. If  $\sigma < 3/2$ , long-range interactions occur, according to mean field theory. For the tricritical point, the critical exponents are:  $\beta = 0.25$ ,  $\gamma = 1$ , and  $\delta = 5$  [46]. The tricritical point sets a boundary between two different ranges of order

phase transitions (first order and second order). These exponents can be generalized into following equations [43]:

$$M_S(T) = M_0 (-\varepsilon)^\beta, T < T_C, \quad (5)$$

$$\chi^{-1}(T) = \left(\frac{h_0}{M_0}\right) \varepsilon^\gamma, T > T_C, \quad (6)$$

$$M = D (\mu_0 H^{1/\delta}), T = T_C, \quad (7)$$

where  $\varepsilon$  is the reduced temperature  $(T - T_C)/T_C$  and  $M_0, h_0/M_0$ , and  $D$  are critical amplitudes.

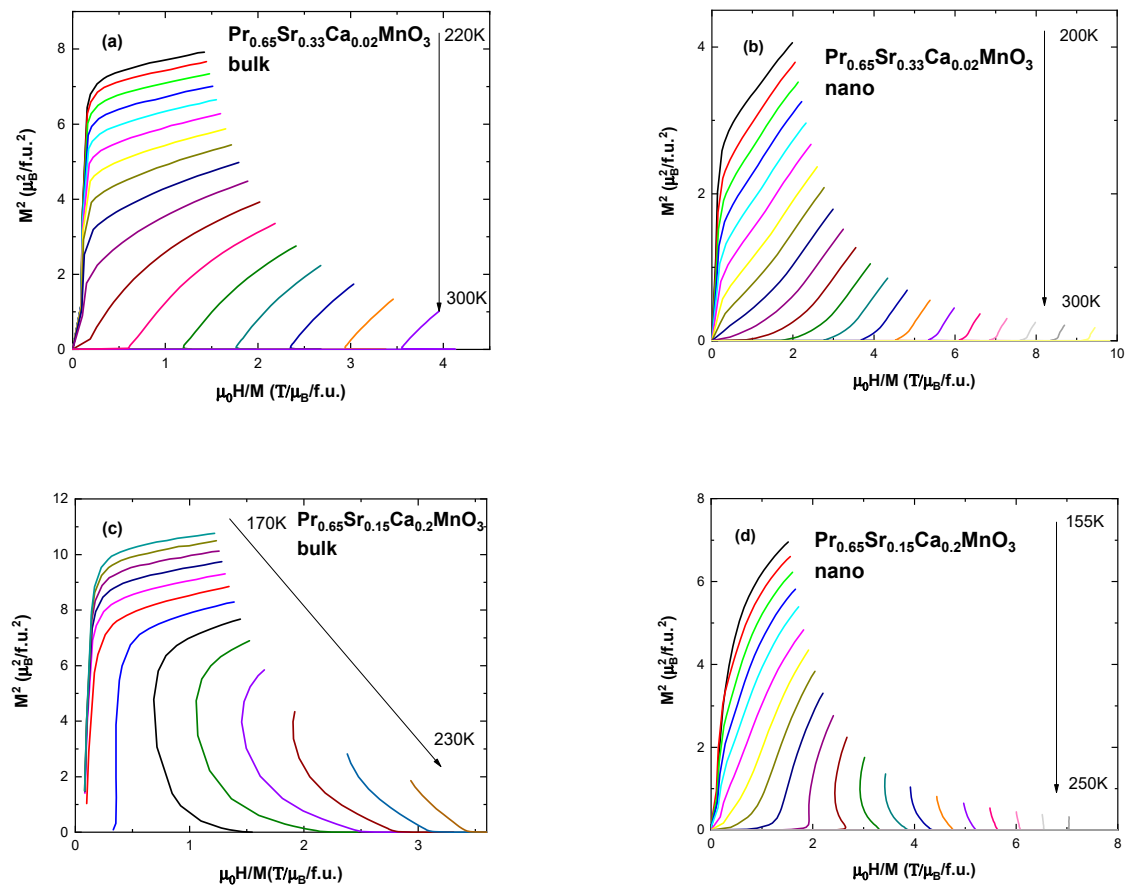


**Figure 7.** Arrott plot ( $M^2$  vs.  $H/M$ ) for (a) the bulk sample with  $x = 0.02$ ; (b) the nanocrystalline sample with  $x = 0.02$ ; (c) bulk sample with  $x = 0.2$ ; (d) nanocrystalline sample  $x = 0.2$ .

To find the proper exponents, we constructed Arrott–Noakes plots by implementing the Modified Arrott plot (MAP) method [43]. It is an iterative method. It includes, at first, construction of Arrott–Noakes plots by choosing exponents which produce straight parallel lines, with the line at  $T_C$  crossing at the origin. Secondly, we find intercepts of lines around  $T_C$ ; on the abscissa, above Curie temperature, to obtain the values of  $\chi_0^{-1}$  and on the ordinate, below  $T_C$ , to find the values of  $M_S$ . Finally, these values are plugged into the Equations (5) and (6) to obtain new values of  $\beta$  and  $\gamma$ . This process is repeated until results stabilize. The exponent  $\delta$  is found using the Widom relation:  $\beta + \gamma = \beta \delta$  [10]. Selected MAP graphs are shown in Figure 8. Full results for MAP are presented in Table 5.

Remarkably, polycrystalline samples are more closely governed by tricritical mean field model ( $\beta = 0.212$ ,  $\gamma = 1.057$ ,  $\delta = 5.986$  for  $x = 0.02$ ), rather than 3D Heisenberg model as reported for other manganites in the literature [10,47]. Sample  $x = 0.3$  does not exhibit ferromagnetic behavior in the high temperature range, only showing small magnetization at low temperatures due to FM clusters and Praseodymium ions, therefore, no critical values

are presented in this work. Alternatively, all critical exponents for nano-sized particles fall within the mean field model values ( $\beta = 0.541, \gamma = 1.01, \delta = 2.867$  for  $x = 0.02$ ) which is comparable to reported values in  $\text{La}_{0.7}\text{Ba}_{0.3-x}\text{Ca}_x\text{MnO}_3$  compounds [22]. Similarly, to the bulk, critical values for nano-sized sample  $x = 0.3$  are not presented.

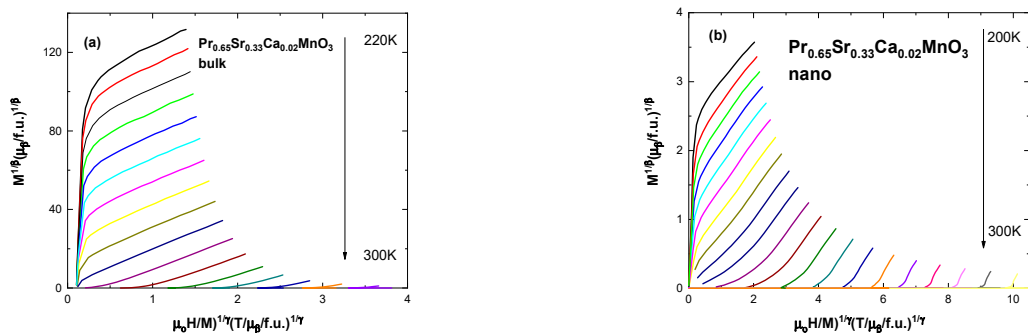


**Figure 8.** Modified Arrott plots for (a) the bulk sample  $x = 0.02$  with  $\beta = 0.212, \gamma = 1.057, \delta = 5.986$  and for (b) the nanocrystalline sample  $x = 0.02$  with  $\beta = 0.541, \gamma = 1.01, \delta = 2.867$ .

**Table 5.** Critical exponent values for all samples from modified Arrott plot method.

Compound		$\gamma$	$\beta$	$\delta$	$T_C$ (K)
$x = 0.02$	bulk	1.057	0.212	5.986	273
$x = 0.05$	bulk	0.981	0.232	5.228	261
$x = 0.1$	bulk	0.985	0.25	4.94	244
$x = 0.2$	bulk	1.036	0.217	5.774	201
$x = 0.3$	bulk	-	-	-	-
$x = 0$	nano	1.023	0.552	2.853	257
$x = 0.02$	nano	1.01	0.541	2.867	252
$x = 0.05$	nano	0.986	0.508	2.941	249
$x = 0.1$	nano	0.977	0.512	2.908	239
$x = 0.2$	nano	0.967	0.531	2.821	191
$x = 0.3$	nano	-	-	-	-
Mean field model		1	0.5	3	
3D Heisenberg model		1.366	0.355	4.8	
Ising model		1.24	0.325	4.82	
Tricritical mean field model		1	0.25	5	

The Kouvel–Fisher (KF) method for determining critical exponents is a widely implemented tool for ferromagnetic materials [47–49]. We used KF to confirm the results from MAP as the two methods are regarded to be very accurate and reliable [47]. Akin to MAP, it is also an iterative method. It requires the construction of Arrott–Noakes plot, finding the intercepts on ordinate and abscissa and fitting these values in the equations [47,49]:

$$M_s \{dM_s/dT\}^{-1} = (T - T_C)/\beta \tag{8}$$

$$\chi_0^{-1} \{d\chi_0^{-1}/dT\}^{-1} = (T - T_C)/\gamma \tag{9}$$

Ideally, plot of  $M_s \{dM_s/dT\}^{-1}$  vs.  $T$  is a straight line with slope =  $1/\beta$  and the intercept giving  $T_C/\beta$ . Same logic applies to the plot of  $\chi_0^{-1} \{d\chi_0^{-1}/dT\}^{-1}$  vs.  $T$  which gives slope equal to  $1/\gamma$ . We present, in Figure 9, selected examples of results from KF

calculations compared to results from MAP for the same compounds. It is evident, that the lines in KF plots are close to being straight and their slope values result in  $\beta$  and  $\gamma$  being close to results from MAP.

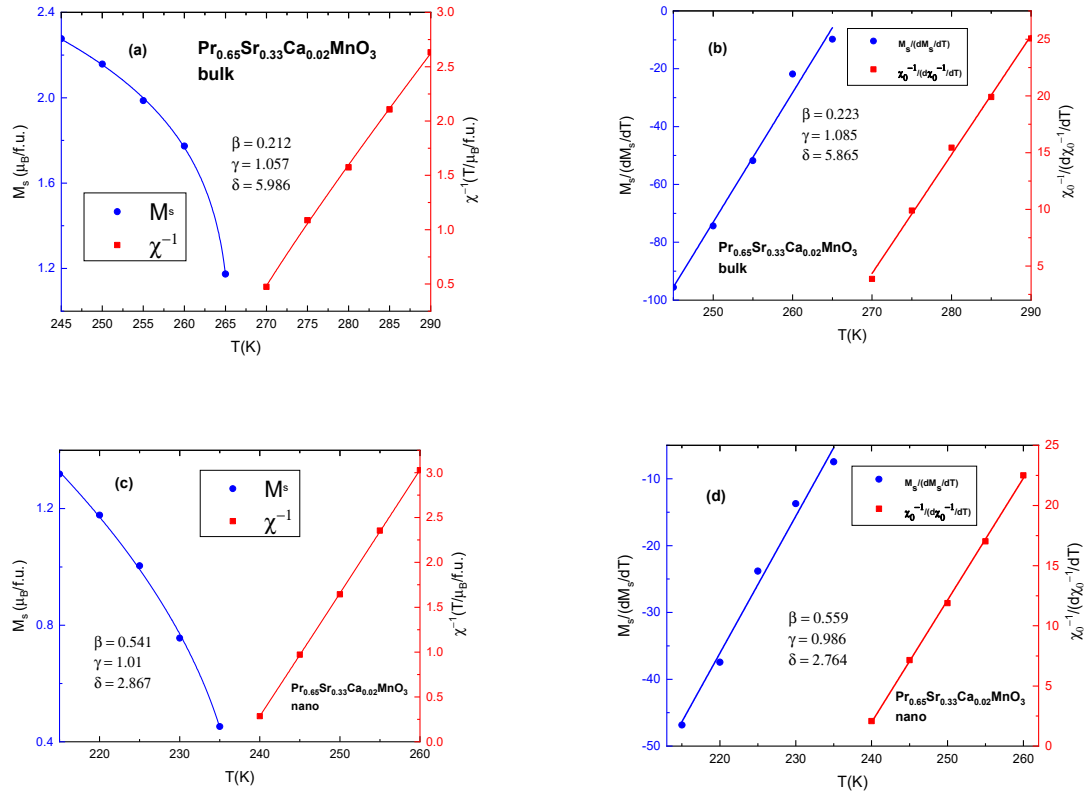


**Figure 9.** Calculated values for critical exponents for (a) MAP analysis for the bulk sample with  $x = 0.02$  (b) KF analysis for the bulk sample with  $x = 0.02$ . (c) MAP analysis for the nanocrystalline sample  $x = 0.02$  (d) KF analysis for nanocrystalline sample  $x = 0.02$ .

Magnetic entropy change was calculated using the following formula [50,51]:

$$\Delta S_m(T, H_0) = S_m(T, H_0) - S_m(T, 0) = \frac{1}{\Delta T} \int_0^{H_0} [M(T + \Delta T, H) - M(T, H)] dH, \quad (10)$$

where magnetization  $M(\mu_0 H)$  is taken from isothermal data at fields of 1–4 T.

Plots of  $-\Delta S_M$  vs.  $T$  (temperature) were constructed in order to better estimate magnetocaloric effect of the compounds, including calculations of relative cooling power RCP [51,52]:

$$RCP(S) = -\Delta S_m(T, H) \times \delta T_{FWHM} \quad (11)$$

where  $\delta T_{FWHM}$  is the range of temperature at full width half maximum.

Selected graphs of samples' entropy change are presented in Figure 10. It is noteworthy that, generally, polycrystalline samples exhibit higher maximum entropy change  $-\Delta S_M$  compared to their nano-sized counterparts, as seen in Figure 10a vs. 10b. Bulk compound with  $x = 0.05$  shows  $-\Delta S_M$  (max) = 5.56 J/kgK at 4 T and nano-sized sample shows  $-\Delta S_M$  (max) = 3.25 J/kgK at 4 T. Bulk samples with  $x = 0.1$  and  $x = 0.2$  exhibit high maximum entropy change at 6.9 J/kgK and 9.2 J/kgK respectively. For all samples, maximum entropy change occurs at around their Curie temperature  $T_C$ . It is also important to note that nanocrystalline compounds exhibit wider range of effective temperature  $\delta T_{FWHM}$  at around 40–70 K while bulk samples show range of 20–30 K.

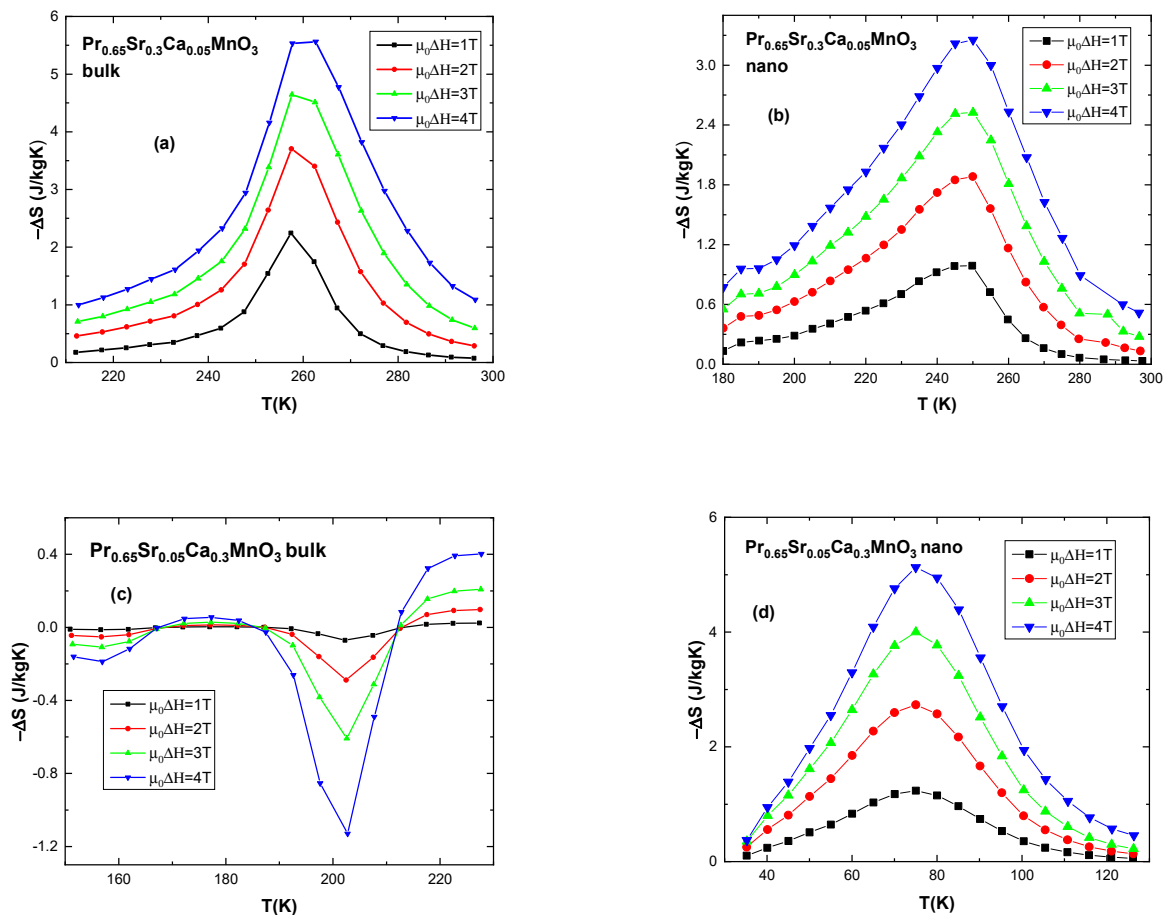


**Figure 10.** Magnetic entropy change vs. temperature for selected samples: (a)  $x = 0.05$  bulk; (b)  $x = 0.05$  nanocrystalline sample; (c)  $x = 0.3$  bulk at AFM-FM; (d)  $x = 0.3$  nanocrystalline at low temperature.

Construction of cooling equipment should not be “blindly” reliant on reported values of RCP [53]; nevertheless, for a long time it has been a useful tool in estimating the applicability of the magnetic material. Although it is the width of the temperature change in nano-sized compounds that is criticized as unreliable, in this work, nanocrystalline compounds deserve attention for their satisfactory level of entropy change, greater or close to  $4 \text{ J}/(\text{kgK})$  for  $\Delta\mu_0H = 4 \text{ T}$ . Both nano-sized and bulk systems exhibit values of entropy change and RCP comparable with other manganites reported in the literature [10,52,54,55].

Delving deeper, unfortunately, RCP tends to overestimate the merits of the materials which have a large temperature range of magnetocaloric effect ( $\delta T_{FWHM}$ ) but small entropy changes [55,56] in no small part because materials with same relative cooling power can behave differently in a magnetic cooling simulation [57]. Moreover, one of the last printed books about magnetic cooling ignores this figure of merit [58].

In order to be of use in magnetic refrigeration applications the chosen materials have to show a large magnetocaloric effect—a large magnetic entropy change. Besides this, there is a list of requirements related with heat transfer, heat capacity, heat conductivity, chemical and mechanical stability, hysteresis losses, eddy currents losses, etc. Therefore, magnetic measurements can be a trusted guide in deciding if a material deserves the effort of complete characterization. Some compounds of the type  $A_{1-x}B_x\text{MnO}_3$  can be considered to be of interest for magnetic refrigeration because some of these compounds show  $-\Delta S_m$  values ( $-\Delta S_m \approx 4\text{--}6 \text{ J}\cdot\text{kg}^{-1}\cdot\text{K}^{-1}$  for  $\Delta H = 5 \text{ T}$ ) comparable to intermetallic alloys [56]. This is the case of our investigated compounds.

The best way to decide the practicality of a material in magnetic cooling applications is by testing directly in a magnetic refrigerator, working on the principle of the AMRR (Active Magnetic Regenerative Refrigeration) cycle [12]. Recent investigations confirmed the

magnetocaloric performance and the potential in magnetic refrigeration of the perovskite oxide  $\text{Pr}_{0.65}\text{Sr}_{0.35}\text{MnO}_3$  [12,59], which has the stoichiometry of our parent compound. When Ca substitutes for Sr in this compound, the magnetic parameters and magnetocaloric effect can be tuned for various temperature applications without significant changes in the magnitude of magnetic entropy change. Our investigations support the bulk polycrystalline  $\text{Pr}_{0.65}\text{Sr}_{(0.35-x)}\text{Ca}_x\text{MnO}_3$  compounds to be promising for magnetic cooling technology, while lower magnitude of magnetocaloric effect in nanocrystalline samples, unfortunately, seems to somewhat hinder their direct practical applications [53,56,57].

Special mention should be made of some feature for samples with  $x = 0.3$ . Both bulk (Figure 10c) and nano-sized (not pictured) compounds exhibit positive entropy change at temperatures associated with antiferromagnetic (CO)/ferromagnetic/paramagnetic phase transition. This phase transition can be observed in the ZFC-FC plots in Figure 6 at around 200–210 K for both samples. As can be observed in Figure 10c, bulk sample exhibits inverse (materials cool down when a magnetic field is adiabatically applied) to normal MCE change suggesting AFM/FM transition, but it seems the changes in the lattice parameters can also modify the magnetic exchange interaction to give rise to a such behavior [60,61]. Additionally, Figure 10d shows a negative entropy change of 5.1 J/kgK at 4 T for nano-sized samples at 75 K. Similar behavior and even higher entropy change is exhibited by the bulk sample at around 40 K (not pictured) at the suppression of the AFM state. These materials can be used to produce both cooling and heating when they are adiabatically demagnetized. Unfortunately, the large values of the magnetic entropy changes can be reach only at low temperatures, far from the range of domestic refrigeration, in the case of these samples.

Low coercivity is of utmost importance in application of cooling materials [51]. All samples exhibit low coercive fields as measured in a hysteresis loop at external fields of up to 4 T at 4 K. Largest coercive field exhibited by a bulk sample is of 190 Oe for  $x = 0.2$ ; with the smallest being 130 Oe for  $x = 0.05$ . Nanocrystalline samples carry larger coercive field compared to polycrystalline samples. It increases with decreasing size of the particles until single domain size. Particles become superparamagnetic with further decrease in size [62]. Largest coercive field is produced by the parent nano-sized with  $x = 0$  at 810 Oe. All values for coercive field and magnetic saturation  $M_s$  are presented in Tables 6 and 7. Nanocrystalline sample  $x = 0.3$  does not reach saturation at 4 T.

**Table 6.** Experimental values for  $\text{Pr}_{0.65}\text{Sr}_{0.35-x}\text{Ca}_x\text{MnO}_3$  bulk materials: magnetic measurements.

Compound (Bulk)	$T_C$ (K)	$M_s$ ( $\mu_B/\text{f.u.}$ )	$H_{ci}$ (Oe)	$ \Delta S_M $	$ \Delta S_M $	RCP (S)	RCP (S)	Refs.
				(J/kgK) $\mu_0\Delta H = 1 \text{ T}$	(J/kgK) $\mu_0\Delta H = 4 \text{ T}$	(J/kg) $\mu_0\Delta H = 1 \text{ T}$	(J/kg) $\mu_0\Delta H = 4 \text{ T}$	
$\text{Pr}_{0.65}\text{Sr}_{0.35}\text{MnO}_3$	295			2.3				[12]
$\text{Pr}_{0.65}\text{Sr}_{0.33}\text{Ca}_{0.02}\text{MnO}_3$	273	3.71	180	2.04	5.53	34	166	This work
$\text{Pr}_{0.65}\text{Sr}_{0.3}\text{Ca}_{0.05}\text{MnO}_3$	261	3.78	170	2.24	5.56	44	167	This work
$\text{Pr}_{0.65}\text{Sr}_{0.25}\text{Ca}_{0.1}\text{MnO}_3$	244	3.94	190	3.03	6.91	45	186	This work
$\text{Pr}_{0.65}\text{Sr}_{0.15}\text{Ca}_{0.2}\text{MnO}_3$	201	3.97	160	4.48	9.21	60	270	This work
$\text{Pr}_{0.65}\text{Sr}_{0.05}\text{Ca}_{0.3}\text{MnO}_3$		3.81	170	4.6 (40 K)	15.3 (40 K)	92 (40 K)	380 (40 K)	This work
$\text{La}_{0.7}\text{Ca}_{0.3}\text{MnO}_3$	256			1.38		41		[10]
$\text{La}_{0.7}\text{Sr}_{0.3}\text{MnO}_3$	365			-	4.44 (5 T)		128 (5 T)	[10]
$\text{La}_{0.6}\text{Nd}_{0.1}\text{Ca}_{0.3}\text{MnO}_3$	233			1.95		37		[10]
$\text{Gd}_5\text{Si}_2\text{Ge}_2$	276			-	18 (5 T)	-	535 (5 T)	[10]
Gd	293			2.8		35		[10]

**Table 7.** Experimental values for  $\text{Pr}_{0.65}\text{Sr}_{0.35-x}\text{Ca}_x\text{MnO}_3$  nano materials.

Compound (Nano)	$T_c$ (K)	$M_s$ ( $\mu_B/\text{f.u.}$ )	$H_{ci}$ (Oe)	$ \Delta S_M $	$ \Delta S_M $	RCP(S)	RCP(S)	Refs.
				(J/kgK) $\mu_0\Delta H = 1 \text{ T}$	(J/kgK) $\mu_0\Delta H = 4 \text{ T}$	(J/kg) $\mu_0\Delta H = 1 \text{ T}$	(J/kg) $\mu_0\Delta H = 4 \text{ T}$	
$\text{Pr}_{0.65}\text{Sr}_{0.35}\text{MnO}_3$	257	3.6	810	1.62	4.55	54	263	This work
$\text{Pr}_{0.65}\text{Sr}_{0.33}\text{Ca}_{0.02}\text{MnO}_3$	252	3.08	720	0.69	2.5	38	175	This work
$\text{Pr}_{0.65}\text{Sr}_{0.3}\text{Ca}_{0.05}\text{MnO}_3$	249	3.16	540	0.99	3.25	48	178	This work
$\text{Pr}_{0.65}\text{Sr}_{0.25}\text{Ca}_{0.1}\text{MnO}_3$	239	3.49	510	1.41	4.37	39	215	This work
$\text{Pr}_{0.65}\text{Sr}_{0.15}\text{Ca}_{0.2}\text{MnO}_3$	191	3.39	620	1.08	3.9	41	185	This work
$\text{Pr}_{0.65}\text{Sr}_{0.05}\text{Ca}_{0.3}\text{MnO}_3$	-	-	600	1.23(75 K)	5.12(75 K)	48(75 K)	204(75 K)	This work
$\text{La}_{0.67}\text{Ca}_{0.33}\text{MnO}_3$	260				0.97 (5 T)		27 (5 T)	[63]
$\text{Pr}_{0.65}(\text{Ca}_{0.6}\text{Sr}_{0.4})_{0.35}\text{MnO}_3$	220			0.75		21.8		[64]
$\text{La}_{0.6}\text{Sr}_{0.4}\text{MnO}_3$	365			1.5		66		[17]

#### 4. Conclusions

Two sample systems of  $\text{Pr}_{0.65}\text{Sr}_{0.35-x}\text{Ca}_x\text{MnO}_3$  ( $x = 0.02, 0.05, 0.1, 0.2, 0.3$ ) were prepared. Solid state reaction as a method of preparation of polycrystalline compounds resulted in samples with an average 12,000 nm grain size. Sucrose based sol-gel method for production of nanocrystalline samples resulted in particles of an average size of approximately 70 nm. X-ray diffraction measurements revealed a single crystallographic phase for all samples. Rietveld refinement analysis confirmed single phase, orthorhombic (Pbnm) symmetry, diminishing cell volume and Mn–O bond length with increasing Ca substitution. Iodometric titration was implemented on both systems to determine their oxygen content. All bulk samples show oxygen deficiency close to  $\text{O}_{2.93\pm 0.02}$  attributed to the preparation method. All nano-sized samples exhibit small oxygen excess of  $\text{O}_{3.02\pm 0.01}$  or less, credited to the effects of the surface/volume ratio of the particles. Bulk compounds were measured for their electrical properties and revealed a feature at a temperature  $T_{p1}$  associated with high disorder at grain boundaries due to Ca substitution. Additionally, samples with Ca levels  $x = 0.1, 0.2$  exhibit a peak at a temperature  $T_{p2}$  associated with the ferromagnetic-paramagnetic transition. With the increase in applied magnetic field,  $T_{p2}$  tends to become higher and smooth out. The sample with  $x = 0.3$  possesses “infinite” resistance for  $\mu_0H = 0 \text{ T}$  and  $1 \text{ T}$  at around 50 K. Further increase in applied field up to 5 T results in overcoming intergrain resistance and shift in the resistance peak. Negative magnetoresistivity was observed for all bulk samples. The smallest value of MR was 11.99% for  $x = 0.02$  at 2 T at  $T_{p1}$ , while the largest value of MR for  $x = 0.2$  of 51.96% for  $T_{p2}$ . Zero-field cooled–field cooled graphs reveal ferromagnetic behavior for  $x = 0.02, 0.05, 0.01, 0.2$  samples. Both  $x = 0.3$  show ferromagnetic-like behavior at low temperatures and antiferromagnetic behavior at higher temperatures than 80 K, with transition to ferromagnetic to paramagnetic behavior at 210 K. Curie temperature  $T_C$  lowers with each Ca substitution: 273 K for bulk  $x = 0.02$  compared to 295 K for parent compound; 252 K for nano-sized  $x = 0.02$  vs. 257 K for parent compound. Low coercivity was found for all samples. Nanocrystalline samples exhibiting larger coercivity compared to their bulk counterparts: 720 Oe vs. 180 Oe for  $x = 0.02$ . Arrott plots confirm second order phase transition for all samples except for  $x = 0.3$ . Modified Arrott plot (MAP) analysis disclosed critical behavior. Critical exponents for polycrystalline samples belong to tricritical mean field model while exponents for nano-sized particles belong to mean field model. The Kouvel–Fisher (KF) method for analyzing critical exponents confirmed MAP results. Bulk compounds reveal higher magnetic saturation  $M_s$  and maximum entropy change  $\Delta S_M$  than nano-sized compounds. Bulk sample with  $x = 0.2$  exhibits highest entropy change  $\Delta S_M = 9.21 \text{ J/kgK}$  (4 T) at 204 K. Relative cooling powers (RCP) for equivalent bulk and nano-sized compounds are comparable in value: 166 J/kg vs. 175 J/kg (4 T) for bulk and nano-sized with  $x = 0.02$ . This is due to the wide effective

temperature range of entropy change  $\delta T_{FWHM}$  in nanocrystalline samples. All values of RCP are high and comparable with relevant compounds reported in the literature. Bulk samples with  $x = 0.3$  exhibits positive entropy change at antiferromagnetic-ferromagnetic transition temperature. Magnetic entropy changes and magnetic parameters of the bulk polycrystalline samples indicate them as potential candidates for magnetocaloric materials. Possibly, they can be combined in construction of multistep refrigeration processes to increase their temperature range and effectiveness. The nanocrystalline samples, which show comparatively lower maximum entropy change are moved to the immediate background of the picture of usable magnetocaloric compounds but could, possibly, be still useful in future developments.

**Author Contributions:** R.A., conceptualization, investigation, methodology, writing—original draft, writing—review and editing, visualization, supervision; D.A., R.H., R.B., G.S., A.S. and L.B.-T., methodology, investigation, review and editing; I.G.D., conceptualization, investigation, methodology, visualization, supervision, review and editing. All authors have read and agreed to the published version of the manuscript.

**Funding:** This research received no external funding.

**Data Availability Statement:** Data presented in this study are available in this article.

**Acknowledgments:** The authors acknowledge the Institute of Physics “Ioan Ursu” of Faculty of Physics from Babes Bolyai University for assistance.

**Conflicts of Interest:** The authors declare no conflict of interest.

## References

1. McKay, C.P. Requirements and limits for life in the context of exoplanets. *Proc. Natl. Acad. Sci. USA* **2014**, *111*, 12628–12633. [[CrossRef](#)] [[PubMed](#)]
2. Briley, G.C. A History of Refrigeration. *Ashrae J.* **2004**, *46*, S31–S34.
3. Gschneidner, K.A.; Pecharsky, V.K. Thirty Years of near Room Temperature Magnetic Cooling: Where We Are Today and Future Prospects. *Int. J. Refrig.* **2008**, *31*, 945–961. [[CrossRef](#)]
4. Salazar-Munoz, V.E.; Lobo Guerrero, A.; Palomares-Sanchez, S.A. Review of magnetocaloric properties in lanthanum manganites. *J. Magn. Magn. Mater.* **2022**, *562*, 169787. [[CrossRef](#)]
5. Smith, A. Who discovered the magnetocaloric effect? *EPJH* **2013**, *38*, 507–517. [[CrossRef](#)]
6. Dagotto, E.; Hotta, T.; Moreo, A. Colossal Magnetoresistant Materials: The Key Role of Phase Separation. *Phys. Rep.* **2001**, *344*, 1–153. [[CrossRef](#)]
7. Pavarini, E.; Koch, E.; Anders, F.; Jarrell, M. *Correlated Electrons: From Models to Materials Modeling and Simulation*; Forschungszentrum Jülich: Jülich, Germany, 2012; Chapter 7, Volume 2, pp. 18–21, ISBN 978-3-89336-796-2.
8. Coey, J.M.D.; Viret, M.; Von Molnár, S. Mixed-Valence Manganites. *Adv. Phys.* **1999**, *48*, 167–293. [[CrossRef](#)]
9. Rostamnejadi, A.; Venkatesan, M.; Alaria, J.; Boese, M.; Kameli, P.; Salamati, H.; Coey, J.M.D. Conventional and Inverse Magnetocaloric Effects in  $\text{La}_{0.45}\text{Sr}_{0.55}\text{MnO}_3$  Nanoparticles. *J. Appl. Phys.* **2011**, *110*, 043905. [[CrossRef](#)]
10. Varvescu, A.; Deac, I.G. Critical Magnetic Behavior and Large Magnetocaloric Effect in  $\text{Pr}_{0.67}\text{Ba}_{0.33}\text{MnO}_3$  Perovskite Manganite. *Phys. B Condens. Matter* **2015**, *470–471*, 96–101. [[CrossRef](#)]
11. Badea, C.; Tetean, R.; Deac, I.G. Suppression of Charge and Antiferromagnetic Ordering in Ga-doped  $\text{La}_{0.4}\text{Ca}_{0.6}\text{MnO}_3$ . *Rom. J. Phys.* **2018**, *63*, 604.
12. Guillou, F.; Legait, U.; Kedous-Lebouc, A.; Hardy, V. Development of a new magnetocaloric material used in a magnetic refrigeration device. *EPJ Web Conf.* **2012**, *29*, 21. [[CrossRef](#)]
13. Licci, F.; Turilli, G.; Ferro, P. Determination of Manganese Valence in Complex La-Mn Perovskites. *J. Magn. Magn. Mater.* **1996**, *164*, L268–L272. [[CrossRef](#)]
14. Zhang, X.H.; Li, Z.Q.; Song, W.; Du, X.W.; Wu, P.; Bai, H.L.; Jiang, H.Y. Magnetic properties and charge ordering in  $\text{Pr}_{0.75}\text{Na}_{0.25}\text{MnO}_3$  manganite. *Solid State Commun.* **2005**, *135*, 356. [[CrossRef](#)]
15. Rao, C.N.R. Charge, Spin, and Orbital Ordering in the Perovskite Manganates,  $\text{Ln}_{1-x}\text{A}_x\text{MnO}_3$  (Ln = Rare Earth, A = Ca or Sr). *J. Phys. Chem. B* **2000**, *104*, 5877–5889. [[CrossRef](#)]
16. Tali, R. Determination of Average Oxidation State of Mn in  $\text{ScMnO}_3$  and  $\text{CaMnO}_3$  by Using Iodometric Titration. *Damascus Univ. J. Basic Sci.* **2007**, *23*, 9–19.
17. Ehsani, M.H.; Kameli, P.; Ghazi, M.E.; Razavi, F.S.; Taheri, M. Tunable magnetic and magnetocaloric properties of  $\text{La}_{0.6}\text{Sr}_{0.4}\text{MnO}_3$  nanoparticles. *J. Appl. Phys.* **2013**, *114*, 223907. [[CrossRef](#)]
18. Dagotto, E. *Nanoscale Phase Separation and Colossal Magnetoresistance*, 1st ed.; Springer Science & Business Media: New York, NY, USA, 2002; pp. 271–284.

19. Raju, K.; Manjunathrao, S.; Venugopal Reddy, P. Correlation between Charge, Spin and Lattice in La-Eu-Sr Manganites. *J. Low Temp. Phys.* **2012**, *168*, 334–349. [[CrossRef](#)]
20. Rao, C.N.R. Perovskites. In *Encyclopedia of Physical Science and Technology*; Elsevier: Amsterdam, The Netherlands, 2003; pp. 707–714.
21. Nath, D.; Singh, F.; Das, R. X-ray Diffraction Analysis by Williamson-Hall, Halder-Wagner and Size-Strain Plot Methods of CdSe Nanoparticles—A Comparative Study. *Mater. Chem. Phys.* **2020**, *239*, 2764–2772. [[CrossRef](#)]
22. Atanasov, R.; Bortnic, R.; Hirian, R.; Covaci, E.; Frentiu, T.; Popa, F.; Iosif Grigore Deac, I.G. Magnetic and Magnetocaloric Properties of Nano- and Polycrystalline Manganites  $\text{La}_{(0.7-x)}\text{Eu}_x\text{Ba}_{0.3}\text{MnO}_3$ . *Materials* **2022**, *15*, 7645. [[CrossRef](#)]
23. Saw, A.K.; Channagoudra, G.; Hunagund, S.; Hadimani, R.L.; Dayal, V. Study of transport, magnetic and magnetocaloric properties in  $\text{Sr}^{2+}$  substituted praseodymium manganite. *Mater. Res. Express* **2020**, *7*, 016105. [[CrossRef](#)]
24. Deac, I.G.; Tetean, R.; Burzo, E. Phase Separation, Transport and Magnetic Properties of  $\text{La}_{2/3}\text{A}_{1/3}\text{Mn}_{1-x}\text{Co}_x\text{O}_3$ , A = Ca, Sr ( $0.5 \leq x \leq 1$ ). *Phys. B Condens. Matter* **2008**, *403*, 1622–1624. [[CrossRef](#)]
25. Panwar, N.; Pandya, D.K.; Agarwal, S.K. Magneto-Transport and Magnetization Studies of  $\text{Pr}_{2/3}\text{Ba}_{1/3}\text{MnO}_3\text{:Ag}_2\text{O}$  Composite Manganites. *J. Phys. Condens. Matter* **2007**, *19*, 456224. [[CrossRef](#)]
26. Panwar, N.; Pandya, D.K.; Rao, A.; Wu, K.K.; Kaurav, N.; Kuo, Y.K.; Agarwal, S.K. Electrical and Thermal Properties of  $\text{Pr}_{2/3}(\text{Ba}_{1-x}\text{Cs}_x)_{1/3}\text{MnO}_3$  Manganites. *Eur. Phys. J. B* **2008**, *65*, 179–186. [[CrossRef](#)]
27. Ibrahim, N.; Rusop, N.A.M.; Rozilah, R.; Asmira, N.; Yahya, A.K. Effect of grain modification on electrical transport properties and electroresistance behavior of  $\text{Sm}_{0.55}\text{Sr}_{0.45}\text{MnO}_3$ . *Int. J. Eng. Technol.* **2018**, *7*, 113–117.
28. Kubo, K.; Ohata, N. A Quantum Theory of Double Exchange. *J. Phys. Soc. Jpn.* **1972**, *33*, 21–32. [[CrossRef](#)]
29. Arun, B.; Suneesh, M.V.; Vasundhara, M. Comparative Study of Magnetic Ordering and Electrical Transport in Bulk and Nano-Grained  $\text{Nd}_{0.67}\text{Sr}_{0.33}\text{MnO}_3$  Manganites. *J. Magn. Magn. Mater.* **2016**, *418*, 265–272. [[CrossRef](#)]
30. Peters, J.A. Relaxivity of Manganese Ferrite Nanoparticles. *Prog. Nucl. Magn. Reson. Spectrosc.* **2020**, *120*, 72–94. [[CrossRef](#)] [[PubMed](#)]
31. Maheswar Repaka, D.V. Magnetic Control of Spin Entropy, Thermoelectricity and Electrical Resistivity in Selected Manganites. Ph.D. Thesis, National University of Singapore, Singapore, 2014.
32. Deac, I.G.; Diaz, S.V.; Kim, B.G.; Cheong, S.-W.; Schiffer, P. Magnetic relaxation in  $\text{La}_{0.250}\text{Pr}_{0.375}\text{Ca}_{0.375}\text{MnO}_3$  with varying phase separation. *Phys. Rev. B* **2002**, *64*, 174426. [[CrossRef](#)]
33. Deac, I.G.; Mitchell, J.; Schiffer, P. Phase Separation and the Low-Field Bulk Magnetic Properties of  $\text{Pr}_{0.7}\text{Ca}_{0.3}\text{MnO}_3$ . *Phys. Rev. B* **2001**, *63*, 172408. [[CrossRef](#)]
34. Sudyoadsuka, T.; Suryanarayananb, R.; Winotaia, P.; Wengerc, L.E. Suppression of charge-ordering and appearance of magnetoresistance in a spin-cluster glass manganite  $\text{La}_{0.3}\text{Ca}_{0.7}\text{Mn}_{0.8}\text{Cr}_{0.2}\text{O}_3$ . *J. Magn. Magn. Mater.* **2004**, *278*, 96–106. [[CrossRef](#)]
35. Anuradha, K.N.; Rao, S.S.; Bhat, S.V. Complete ‘melting’ of charge order in hydrothermally grown  $\text{Pr}_{0.57}\text{Ca}_{0.41}\text{Ba}_{0.02}\text{MnO}_3$  nanowires. *J. Nanosci. Nanotechnol.* **2007**, *7*, 1775–1778. [[CrossRef](#)]
36. Rao, S.S.; Tripathi, S.; Pandey, D.; Bhat, S.V. Suppression of charge order, disappearance of antiferromagnetism, and emergence of ferromagnetism in  $\text{Nd}_{0.5}\text{Ca}_{0.5}\text{MnO}_3$  nanoparticles. *Phys. Rev. B* **2006**, *74*, 144416. [[CrossRef](#)]
37. Lu, C.L.; Dong, S.; Wang, K.F.; Gao, F.; Li, P.L.; Lv, L.Y.; Liu, J.M. Charge-order breaking and ferromagnetism in  $\text{La}_{0.4}\text{Ca}_{0.6}\text{MnO}_3$  nanoparticles. *Appl. Phys. Lett.* **2007**, *91*, 032502. [[CrossRef](#)]
38. Hüser, D.; Wenger, L.E.; van Duynvelt, A.J.; Mydosh, J.A. Dynamical behavior of the susceptibility around the freezing temperature in  $(\text{Eu,Sr})\text{S}$ . *Phys. Rev. B* **1983**, *27*, 3100. [[CrossRef](#)]
39. Cao, G.; Zhang, J.; Wang, S.; Yu, J.; Jing, C.; Cao, S.; Shen, X. Reentrant spin glass behavior in CE-type AFM  $\text{Pr}_{0.5}\text{Ca}_{0.5}\text{MnO}_3$  manganite. *J. Magn. Magn. Mater.* **2007**, *310*, 169. [[CrossRef](#)]
40. Jeddi, M.; Gharsallah, H.; Bejar, M.; Bekri, M.; Dhahri, E.; Hlil, E.K. Magnetocaloric Study, Critical Behavior and Spontaneous Magnetization Estimation in  $\text{La}_{0.6}\text{Ca}_{0.3}\text{Sr}_{0.1}\text{MnO}_3$  Perovskite. *RSC Adv.* **2018**, *8*, 9430–9439. [[CrossRef](#)]
41. Arrott, A. Criterion for Ferromagnetism from Observations of Magnetic Isotherms. *Phys. Rev.* **1957**, *108*, 1394–1396. [[CrossRef](#)]
42. Banerjee, B.K. On a Generalised Approach to First and Second Order Magnetic Transitions. *Phys. Lett.* **1964**, *12*, 16–17. [[CrossRef](#)]
43. Arrott, A.; Noakes, J.E. Approximate Equation of State for Nickel Near Its Critical Temperature. *Phys. Rev. Lett.* **1967**, *19*, 786–789. [[CrossRef](#)]
44. Stanley, H.E. *Introduction to Phase Transitions and Critical Phenomena*; Oxford University Press: Oxford, UK, 1987; pp. 7–10.
45. Fisher, M.E.; Ma, S.K.; Nickel, B.G. Critical Exponents for Long-Range Interactions. *Phys. Rev. Lett.* **1972**, *29*, 917. [[CrossRef](#)]
46. Pathria, R.K.; Beale, P.D. Phase Transitions: Criticality, Universality, and Scaling. In *Statistical Mechanics*; Elsevier: Amsterdam, The Netherlands, 2022; pp. 417–486.
47. Vadnala, S.; Asthana, S. Magnetocaloric effect and critical field analysis in Eu substituted  $\text{La}_{0.7-x}\text{Eu}_x\text{Sr}_{0.3}\text{MnO}_3$  ( $x = 0.0, 0.1, 0.2, 0.3$ ) manganites. *J. Magn. Magn. Mater.* **2018**, *446*, 68–79. [[CrossRef](#)]
48. Kim, D.; Revaz, B.; Zink, B.L.; Hellman, F.; Rhyne, J.J.; Mitchell, J.F. Tri-critical Point and the Doping Dependence of the Order of the Ferromagnetic Phase Transition of  $\text{La}_{1-x}\text{Ca}_x\text{MnO}_3$ . *Phys. Rev. Lett.* **2002**, *89*, 227202. [[CrossRef](#)] [[PubMed](#)]
49. Pelka, R.; Konieczny, P.; Fitta, M.; Czaplá, M.; Zielinski, P.M.; Balanda, M.; Wasiutynski, T.; Miyazaki, Y.; Inaba, A.; Pinkowicz, D.; et al. Magnetic systems at criticality: Different signatures of scaling. *Acta Phys. Pol.* **2013**, *124*, 977. [[CrossRef](#)]
50. Souca, G.; Iamandi, S.; Mazilu, C.; Dudric, R.; Tetean, R. Magnetocaloric Effect and Magnetic Properties of  $\text{Pr}_{1-x}\text{Ce}_x\text{Co}_3$  Compounds. *Stud. Univ. Babeş-Bolyai Phys.* **2018**, *63*, 9–18. [[CrossRef](#)]

51. Zverev, V.; Tishin, A.M. Magnetocaloric Effect: From Theory to Practice. In *Reference Module in Materials Science and Material Engineering*; Elsevier: Amsterdam, The Netherlands, 2016; pp. 5035–5041. [[CrossRef](#)]
52. Deac, I.G.; Vladescu, A. Magnetic and magnetocaloric properties of  $\text{Pr}_{1-x}\text{Sr}_x\text{CoO}_3$  cobaltites. *J. Magn. Magn. Mater.* **2014**, *365*, 1–7. [[CrossRef](#)]
53. Griffith, L.D.; Mudryk, Y.; Slaughter, J.; Pecharsky, V.K. Material-based figure of merit for caloric materials. *J. Appl. Phys.* **2018**, *123*, 034902. [[CrossRef](#)]
54. Naik, V.B.; Barik, S.K.; Mahendiran, R.; Raveau, B. Magnetic and Calorimetric Investigations of Inverse Magnetocaloric Effect in  $\text{Pr}_{0.46}\text{Sr}_{0.54}\text{MnO}_3$ . *Appl. Phys. Lett.* **2011**, *98*, 112506. [[CrossRef](#)]
55. Gong, Z.; Xu, W.; Liedienov, N.A.; Butenko, D.S.; Zatonovskiy, I.V.; Gural'skiy, I.A.; Wei, Z.; Li, Q.; Liu, B.; Batman, Y.A.; et al. Expansion of the multifunctionality in off-stoichiometric manganites using post-annealing and high pressure: Physical and electrochemical studies. *Phys. Chem. Chem. Phys.* **2002**, *24*, 21872–21885. [[CrossRef](#)]
56. Sandeman, K.G. Magnetocaloric materials: The search for new systems. *Scr. Mater.* **2012**, *67*, 566–571. [[CrossRef](#)]
57. Smith, A.; Bahl, A.C.R.H.; Bjørk, R.; Engelbrecht, K.; Kaspar, K.; Nielsen, K.K.; Pryds, N. Materials challenges for high performance magnetocaloric refrigeration devices. *Adv. Energy Mater.* **2012**, *2*, 1288–1318. [[CrossRef](#)]
58. Kitanovski, A.; Tusek, J.; Tomc, U.; Plaznik, U.; Ozbolt, M.; Poredos, A. *Magnetocaloric Energy Conversion: From Theory to Applications*, 1st ed.; Springer: Cham, Switzerland, 2015. [[CrossRef](#)]
59. Legait, U.; Guillou, F.; Kedous-Lebouc, A.; Hardy, A.V.; Almanza, M. An experimental comparison of four magnetocaloric regenerators using three different materials. *Int. J. Refrig.* **2014**, *37*, 147–155. [[CrossRef](#)]
60. Krishnamoorthi, C.; Barik, S.K.; Siu, Z.; Mahendiran, R. Normal and inverse magnetocaloric effects in  $\text{La}_{0.5}\text{Ca}_{0.5}\text{Mn}_{1-x}\text{Ni}_x\text{O}_3$ . *Solid State Commun.* **2010**, *150*, 1670–1673. [[CrossRef](#)]
61. von Ranke, P.J.; de Oliveira, N.A.; Alho, B.P.; Plaza, E.J.R.; de Sousa, V.S.R.; Caron, L.; Reis, M.S. Understanding the inverse magnetocaloric effect in antiferro- and ferrimagnetic arrangements. *J. Phys. Condens. Matter* **2009**, *21*, 056004. [[CrossRef](#)] [[PubMed](#)]
62. Majumder, D.D.; Majumder, D.D.; Karan, S. Magnetic Properties of Ceramic Nanocomposites. In *Ceramic Nanocomposites*; Banerjee, R., Manna, I., Eds.; Woodhead Publishing Series in Composites Science and Engineering; Elsevier B.V.: Amsterdam, The Netherlands, 2013; pp. 51–91. [[CrossRef](#)]
63. Hueso, L.E.; Sande, P.; Miguéns, D.R.; Rivas, J.; Rivadulla, F.; López-Quintela, M.A. Tuning of the magnetocaloric effect in nanoparticles synthesized by sol–gel techniques. *J. Appl. Phys.* **2002**, *91*, 9943–9947. [[CrossRef](#)]
64. Anis, B.; Tapas, S.; Banerjee, S.; Das, I. Magnetocaloric properties of nanocrystalline  $\text{Pr}_{0.65}(\text{Ca}_{0.6}\text{Sr}_{0.4})_{0.35}\text{MnO}_3$ . *J. Appl. Phys.* **2008**, *103*, 013912. [[CrossRef](#)]

**Disclaimer/Publisher's Note:** The statements, opinions and data contained in all publications are solely those of the individual author(s) and contributor(s) and not of MDPI and/or the editor(s). MDPI and/or the editor(s) disclaim responsibility for any injury to people or property resulting from any ideas, methods, instructions or products referred to in the content.